RESEARCH ARTICL https://doi.org/10.15302/planet.2026.26000

Argon isotope fractionation during hydrodynamic escape from early Mars

***Correspondence:**
youzhou.sim@gmail.com

Received 1 January 2026
Received in revised form 1 January 2026
Accepted 1 January 2026

Citation:
Huang Y., Zhou Y. and Liu Y. X. (2026). Argon isotope fractionation during hydrodynamic escape from early Mars. *Planet* **2**:26000.

Yi Huang, You Zhou (✉), Yixuan Liu

Research Center for Planetary Science, Chengdu University of Technology, Chengdu 610059, China

Intense high-energy irradiation from the young Sun may have driven hydrodynamic escape and fractionated atmospheric Ar isotopes on early Mars. To quantify this process, we couple a one-dimensional radiative-convective atmospheric structure model with multicomponent H–O–CO_2 escape, incorporating energy- and diffusion-limited constraints on the H flux and a composition-dependent heating efficiency. The resulting H outflow determines the differential escape of ^{36}Ar and ^{38}Ar. A global survey of 1023 cases reveals distinct isotope-ratio distributions across solar evolutionary tracks: slow rotators produce the broadest range and lowest ratios, moderate rotators yield a narrower distribution, and fast rotators retain relatively high ratios indicative of weaker fractionation. Refinement with 613 additional cases identifies 32 slow-rotator cases whose modeled early-stage end states fall within the present Martian reference range; no such cases occur along the other tracks. These cases occupy two separated regions of parameter space characterized by relatively large initial H_2O inventories. Sensitivity tests show that composition-dependent heating efficiency modifies fractionation by altering the time the crossover mass spends within the 36–38 amu selective-fractionation window. Together, these results indicate that the contribution of early hydrodynamic escape to Martian Ar isotope fractionation depends strongly on the initial atmospheric state and the young Sun's irradiation history.

Mars, early atmosphere, hydrodynamic escape, Ar isotopes, mass fractionation, heating efficiency

1. Introduction

During the early formation of terrestrial planets, atmospheric compositions were shaped jointly by planetary accretion, magma-ocean outgassing, and atmospheric escape. The H_2O and CO_2 released as a magma ocean cooled and solidified could form a dense steam atmosphere, whose mass and evolutionary timescale depended strongly on the initial volatile inventory and the atmospheric greenhouse effect (Elkins-Tanton, 2008; Lebrun et al., 2013; Marcq et al., 2017). After dispersal of the protoplanetary disk, planetary atmospheres were exposed to the intense X-ray and extreme-ultraviolet irradiation of the young Sun. Heating and expansion of the upper atmosphere could then lead to hydrodynamic escape under favorable conditions. For a weakly bound planet such as Mars, this process may have strongly influenced the retention of early volatiles and the subsequent atmospheric evolution (Lammer et al., 2008; Erkaev et al., 2014; Lammer et al., 2013).

Under intense high-energy irradiation from the young Sun, H produced by the photodissociation of H_2O can escape vigorously. If the hydrogen escape flux is sufficiently large, O, CO_2, and trace noble gases can be collisionally dragged along with the outflow. Whether a heavy species can be efficiently entrained depends on the H flux, gravity, temperature, mixing ratios, and binary diffusion coefficients. Because isotopes of a given element differ in mass, they escape with different efficiencies and consequently undergo mass-dependent isotopic fractionation (Zahnle and Kasting, 1986; Hunten et al., 1987; Zahnle et al., 1990; Odert et al., 2018; Benedikt et al., 2020). For noble gases, the accumulated fractionation depends not only on the evolution of the

This is an open access article under the CC BY license (http://creativecommons.org/licenses/by/4.0).

crossover mass but also on the long-term integration of differential losses over distinct evolutionary stages.

Noble-gas abundances and isotopic compositions preserve records of volatile loss and are therefore widely used to investigate the atmospheric evolution of terrestrial planets (Hunten et al., 1987; Zahnle et al., 1990). Hydrodynamic escape has long been recognized as a possible mechanism for Ar loss and fractionation on early terrestrial planets (Zahnle et al., 1990; Odert et al., 2018). More direct evidence comes from the Martian meteorite record. Willett et al. (2022) inferred that substantial mass-dependent Ar fractionation may already have occurred within the first ~150 Myr of Martian history and identified hydrodynamic escape as a plausible mechanism. More recently, Pahlevan et al. (2025) showed that hydrodynamic escape during early Martian atmospheric evolution can produce both substantial Ar loss and isotopic fractionation. Because Ar is chemically inert, its isotopic evolution is controlled primarily by physical transport and escape rather than atmospheric chemistry. The mass difference between ^{36}Ar and ^{38}Ar therefore provides a sensitive tracer of differential atmospheric loss. Curiosity/SAM measured a present near-surface Martian ^{36}Ar/^{38}Ar ratio of 4.2±0.1 (Atreya et al., 2013; Mahaffy et al., 2013), substantially fractionated relative to more primitive Ar reservoirs.

The modern Martian Ar isotope ratio, however, cannot be attributed to early hydrodynamic escape alone. After the hydrodynamic phase weakened, diffusive separation, sputtering and other nonthermal escape processes, volcanic resupply, and exchange with surface or crustal reservoirs continued to modify both the abundance and isotopic composition of atmospheric Ar. Long-term evolution models and MAVEN observations indicate that these later processes can remove substantial amounts of Ar and further decrease atmospheric ^{36}Ar/^{38}Ar (Slipski and Jakosky, 2016; Jakosky et al., 2017). At the same time, the meteorite record suggests that appreciable Ar fractionation was already established early in Martian history (Willett et al., 2022). The present isotopic composition is therefore most naturally interpreted as the cumulative outcome of multiple escape stages rather than the signature of a single process. The key question addressed here is how much fractionation early hydrodynamic escape can generate by itself, and how that contribution depends on the initial volatile inventory, atmospheric composition, and high-energy evolution of the young Sun.

To address this question, we develop an early-Martian atmospheric evolution model that couples a one-dimensional radiative–convective structure to multicomponent H–O–CO_2 hydrodynamic escape and tracks the differential loss of ^{36}Ar and ^{38}Ar in the H outflow. We first compare the model with the early-Mars multicomponent escape calculations of Erkaev et al. (2014) to test the treatment of background-atmosphere escape and time integration. We then examine how Ar isotope fractionation varies with the initial total volatile pressure $P_{\rm vol}$, the CO_2 pressure fraction ϕ_{CO_2}, and different high-energy evolutionary histories of the young Sun, and assess how composition-dependent heating efficiency modifies the fractionation outcome. This study therefore quantifies the potential contribution and parameter dependence of early hydrodynamic escape to Martian Ar isotope fractionation; explicit coupling to later nonthermal escape and atmospheric resupply lies beyond the present scope.

2. Methods

We investigate Ar isotope fractionation during hydrodynamic escape from an early Martian H_2O–CO_2 atmosphere. Our model couples a one-dimensional radiative–convective atmospheric structure (Marcq et al., 2017) to multicomponent escape of H, O, and CO_2 (Odert et al., 2018; Wang et al., 2025). At each timestep, the atmospheric structure is updated from the evolving H_2O and CO_2 inventories. Hydrogen escape is constrained by both the energy-limited rate (Watson et al., 1981) and the diffusion-limited supply (Wordsworth and Pierrehumbert, 2013), with a composition-dependent effective heating efficiency adopted in the energy-limited calculation (Zahnle and Kasting, 2023). The resulting H outflow is then used to calculate the crossover mass of the Ar isotopes (Hunten et al., 1987), which in turn determines the differential entrainment and isotopic fractionation of ^{36}Ar and ^{38}Ar. Following the escape calculation, the species inventories are updated and returned to the atmospheric calculation, allowing the Ar isotopic composition to be followed throughout the early hydrodynamic escape stage.

2.1. Atmospheric structure and multicomponent hydrodynamic escape

At each time step, the partial pressures are calculated from the current atmospheric inventories of H_2O and CO_2 and passed to the one-dimensional radiative–convective model of Marcq et al. (2017) to update the vertical pressure–temperature structure. Following Wang et al. (2025), the 1 μbar pressure level is adopted as the base of hydrodynamic escape, with radius

$$r_0 = R_{\rm Mars} + z, \tag{1}$$

where $R_{\rm Mars}$ is the radius of Mars and z is the altitude of the 1μ bar pressure level obtained from the pressure–altitude profile. The gravitational potential per unit mass and the local gravitational acceleration at the escape base are

$$\Delta\Phi = \frac{GM_{\rm Mars}}{r_0}, \tag{2}$$

and

$$g = \frac{GM_{\rm Mars}}{r_0^2}. \tag{3}$$

Thus, as the atmospheric structure evolves, r_0 changes accordingly, and both the gravitational potential $\Delta\Phi$ and the local gravity g at the escape base are updated consistently with it.

The molecular fractions of H_2O and CO_2 are defined as

$$\chi_{\rm H_2O} = \frac{N_{\rm H_2O}}{N_{\rm H_2O} + N_{\rm CO_2}}. \tag{4}$$

and

$$\chi_{\rm CO_2} = \frac{N_{\rm CO_2}}{N_{\rm H_2O} + N_{\rm CO_2}}. \tag{5}$$

To represent the effect of atmospheric composition on the efficiency of EUV-driven escape, the effective heating efficiency is parameterized following Zahnle and Kasting (2023),

$$\eta_{\rm eff} = \eta_0 \frac{3\chi_{\rm H_2O}}{1 + 3\chi_{\rm H_2O}}, \tag{6}$$

where $\eta_0 = 0.20$ is a fixed reference parameter that sets the overall scale of the effective heating efficiency and is not fitted to the Ar-isotope results. In the pure-H_2O limit ($\chi_{\rm H_2O} = 1$), this parameterization gives $\eta_{\rm eff} = 0.15$, consistent with values used in previous early-Mars hydrodynamic-escape calculations (Erkaev et al., 2014). As the relative proportions of H_2O and CO_2 evolve, $\eta_{\rm eff}$ is recalculated at every time step and used to determine the corresponding energy-limited escape flux.

The EUV flux received by Mars is calculated as

$$F_{\rm EUV}(t) = \frac{L_{\rm EUV}(t)}{4\pi d_{\rm Mars}^2}, \tag{7}$$

where $d_{\rm Mars}$ is the orbital distance of Mars. The time evolution of $L_{\rm EUV}$ follows the young-Sun rotational tracks of Tu et al. (2015). Solar rotation enters the model through these prescribed $L_{\rm EUV}(t)$ histories, with the slow-rotator track leaving the high-energy saturated regime earlier than the moderate- and fast-rotator tracks.

We first determine the multicomponent H–O–CO_2 escape permitted by the available EUV energy. The energy-limited condition is written as (Watson et al., 1981)

$$\frac{\eta_{\rm eff} F_{\rm EUV}}{4\Delta\Phi} = m_{\rm H}F_{\rm H} + m_{\rm O}F_{\rm O} + m_{\rm CO_2}F_{\rm CO_2}, \tag{8}$$

where F_i and m_i are the particle escape flux per unit area evaluated at the effective escape base r_0 and the particle mass, respectively, of species i.

The H and O particle inventories used in the escape calculation are derived from the evolving H_2O inventory, whereas CO_2 is treated as a molecular species. We assume that the atmosphere below the escape base remains well mixed, so the escape flux of a heavier species i is expressed as

$$F_i = F_{\rm H} f_i x_i, \tag{9}$$

where f_i is the abundance of species i relative to H and x_i is its fractionation factor.

For O,

$$f_{\rm O} = \frac{N_{\rm O}}{N_{\rm H}}, \tag{10}$$

and

$$x_{\rm O} = 1 - \frac{g(m_{\rm O} - m_{\rm H})b_{\rm H,O}}{F_{\rm H}k_{\rm B}T(1 + f_{\rm O})}. \tag{11}$$

For CO_2,

$$f_{\rm CO_2} = \frac{N_{\rm CO_2}}{N_{\rm H}}, \tag{12}$$

and

$$x_{\rm CO_2} = \frac{1 - \frac{g(m_{\rm CO_2} - m_{\rm H})b_{\rm H,CO_2}}{F_{\rm H}k_{\rm B}T} + \frac{b_{\rm H,CO_2}}{b_{\rm H,O}} f_{\rm O}(1 - x_{\rm O}) + \frac{b_{\rm H,CO_2}}{b_{\rm O,CO_2}} f_{\rm O} x_{\rm O}}{1 + \frac{b_{\rm H,CO_2}}{b_{\rm O,CO_2}} f_{\rm O}}. \tag{13}$$

These multicomponent drag relations follow previous hydrodynamic-escape treatments (Odert et al., 2018; Benedikt et al., 2020). Here $b_{i,j}$ s the binary diffusion parameter, $k_{\rm B}$ is the Boltzmann constant, and T is the temperature of escape base.

Combining the energy balance with the heavy species drag relations gives the energy-limited candidate H escape flux,

$$F_{\rm H,EL} = \frac{\eta_{\rm eff} F_{\rm EUV}}{4\Delta\Phi\left(m_{\rm H} + m_{\rm O} f_{\rm O} x_{\rm O} + m_{\rm CO_2} f_{\rm CO_2} x_{\rm CO_2}\right)}. \tag{14}$$

Because x_O and x_{CO_2} themselves depend on the H flux, $F_{H,EL}$ and the associated heavy species fractionation factors must be determined self-consistently.

The energy-limited rate specifies the H escape flux permitted by the available EUV energy, but the actual flux can also be constrained by the rate at which hydrogen-bearing material is transported to the upper atmosphere. We calculate the H_2O mixing ratio at the cold trap from the one-dimensional atmospheric structure and use an H_2O–CO_2 binary diffusion treatment to estimate the maximum upward transport flux of H_2O. The diffusion-limited H_2O flux at the cold trap is (Wordsworth and Pierrehumbert, 2013)

$$F_{H_2O,DL} = b_{H_2O,CO_2} f_{H_2O,ct}\left(H_{CO_2}^{-1} - H_{H_2O}^{-1}\right), \quad (15)$$

where b_{H_2O,CO_2} is the binary diffusion parameter for H_2O in CO_2, for which we adopt $b_{H_2O,CO_2} = 1.56\times10^{21}\times(T/1000\,\mathrm{K})^{0.75}\ \mathrm{m^{-1}\,s^{-1}}$ based on Marrero & Mason (1972).

The scale height of species j at the cold trap is defined as

$$H_j = \frac{k_B T_{ct}}{m_j g_{ct}}, \quad (16)$$

where T_{ct} and g_{ct} are the cold-trap temperature and local gravity. Assuming that H_2O transported to the upper atmosphere is efficiently photodissociated, the corresponding upper limit on the supply of atomic H is

$$F_{H,DL} = 2F_{H_2O,DL}. \quad (17)$$

The actual H escape flux is therefore

$$F_H = \min\left(F_{H,EL}, F_{H,DL}\right). \quad (18)$$

Once F_H is determined, the O and CO_2 fractionation factors and escape fluxes are recalculated. The diffusion limit controls the supply of H to the escape region, whereas the multicomponent fractionation relations determine the efficiency with which O and CO_2 are entrained by the H outflow.

With the actual H escape flux established, the fractionation factors of O and CO_2 are determined from the corresponding fractionation relations (Eqs. (11) and (13)), and their escape fluxes (Eq. (9)). The diffusion-supply limit controls the H flux available to the escape region, whereas x_O and x_{CO_2} describe the relative entrainment of O and CO_2 by the H outflow. The atmospheric inventories are then updated according to

$$N_i(t+\Delta t) = N_i(t) - 4\pi r_0^2(t) F_i(t)\Delta t. \quad (19)$$

The updated inventories are used in the atmospheric structure and escape calculations at the next timestep, while the resulting H outflow provides the input to the Ar isotope-fractionation calculation in Section 2.2.

2.2. Ar isotope escape and fractionation

The H outflow obtained in Section 2.1 is used to calculate the escape of trace Ar isotopes. Because Ar is a minor constituent of the atmosphere, ^{36}Ar and ^{38}Ar are treated independently in the H–Ar binary approximation, with no feedback from Ar on the bulk H–O–CO_2 escape.

The ability of the H outflow to entrain Ar isotope i is characterized by the crossover mass (Hunten et al., 1987):

$$m_{c,i} = m_H + \frac{k_B T F_H}{b_{H,i} g X_{H,i}}, \quad (20)$$

where $b_{H,i}$ is the binary diffusion parameter between H and Ar isotope i, and $X_{H,i}$ is the H mixing fraction in the H–Ar binary system,

$$X_{H,i} = \frac{N_H}{N_H + N_i}. \quad (21)$$

Because Ar remains a trace constituent, $X_{H,i}$ is close to unity, although the full expression is retained in the calculation. The binary diffusion parameters adopted in the multicomponent escape and Ar isotope calculations are summarized in Table 1 (Zahnle and Kasting, 1986).

The fractionation factor of Ar isotope i relative to H is defined as

$$x_{Ar,i} = \max\left[0, \frac{m_{c,i} - m_i}{m_{c,i} - m_H}\right]. \quad (22)$$

Its abundance relative to H is

$$f_{Ar,i} = \frac{N_{Ar,i}}{N_H}, \quad (23)$$

and the corresponding escape flux is

$$F_{Ar,i} = F_H f_{Ar,i} x_{Ar,i}. \quad (24)$$

When $m_{c,i} \leqslant m_i$, $x_{Ar,i} = 0$ and the isotope is no longer effectively entrained by the H outflow. As the H escape flux and atmospheric state evolve, the crossover mass changes relative to the masses of ^{36}Ar and ^{38}Ar. Their different masses therefore lead to different cumulative losses and, consequently, mass-dependent Ar isotope fractionation (Zahnle et al., 1990).

The inventories of both Ar isotopes are updated according to Eq. (19). The atmospheric Ar isotope ratio is defined as

Table 1 Binary diffusion parameters used in the multicomponent escape calculation.

Species pair	Symbol	Adopted expression
H–O	$b_{H,O}$	$4.8\times10^{19}T^{0.75}$
H–CO_2	b_{H,CO_2}	$8.4\times10^{19}T^{0.60}$
O–CO_2	b_{O,CO_2}	$7.86\times10^{18}T^{0.776}$
H–Ar	$b_{H,Ar}$	$1.06\times10^{20}T^{0.597}$

Note: $b_{i,j}$ is in $m^{-1}\,s^{-1}$, and the temperature T is in K.

$$R_{Ar}(t)=\frac{N_{^{36}Ar}(t)}{N_{^{38}Ar}(t)}. \quad (25)$$

Thus, R_{Ar}(t) represents the cumulative differential loss of ^{36}Ar and ^{38}Ar throughout the early hydrodynamic escape stage. The model initial conditions and the observational reference used in the parameter-space analysis are described in Section 2.3.

2.3. Initial conditions and parameter-space sampling

We characterize the initial H_2O–CO_2 atmosphere using the total volatile pressure P_{vol} and the CO_2 pressure fraction ϕ_{CO_2}, where $P_{vol}=P_{H_2O}+P_{CO_2}$ and $\phi_{CO_2}=P_{CO_2}/P_{vol}$. Based on the early-Mars magma-ocean outgassing studies of Elkins-Tanton (2008) and Erkaev et al. (2014), we consider P_{vol} ranging from 100 to 400 bar and ϕ_{CO_2} ranging from 0.10 to 0.30, with a modest extension toward larger initial volatile inventories to encompass a broader range of initial atmospheric conditions. The sampling intervals are 10 bar in P_{vol} and 0.02 in ϕ_{CO_2}, respectively.

In addition to the initial atmospheric conditions, hydrodynamic escape is strongly influenced by the EUV evolution of the young Sun (Watson et al., 1981; Odert et al., 2018). We therefore apply the slow, moderate, and fast rotator EUV evolutionary tracks of Tu et al. (2015) to each initial atmospheric state. Applying the three solar evolutionary tracks across all sampled atmospheric conditions results in 1023 global simulations. Following Odert et al. (2018), we adopt $t_0=10$ Myr as the integration start time. The integration is terminated once the atmospheric H inventory is no longer sufficient to sustain H-driven hydrodynamic escape. The remaining fixed model parameters and their sources are summarized in Table A1.

Ar is treated as a trace constituent and does not feed back on the bulk H–O–CO_2 escape. The initial relative abundances of ^{36}Ar and ^{38}Ar follow the Solar System isotopic composition compiled by Lodders (2021), while the initial Ar isotope ratio is set to $R_{Ar,0}$=5.2005, corresponding to the solar Ar isotopic composition measured by the Genesis solar-wind mission (Meshik et al., 2014). The atmospheric Ar isotope ratio at the end of the integration is denoted $R_{Ar,end}$.

To compare the magnitude of Ar isotope fractionation produced under different initial conditions, the present Martian atmospheric value, $^{36}Ar/^{38}Ar=4.2\pm0.1$, is adopted as an observational benchmark (Atreya et al., 2013). Cases with final isotope ratios within this observed range are classified as reference-range cases. This benchmark is used only to assess whether early hydrodynamic escape can produce fractionation comparable to the present Martian record, rather than as a required terminal condition, because the Martian Ar isotopic composition also reflects subsequent nonthermal escape and long-term atmospheric evolution (Jakosky et al., 2017; Lichtenegger et al., 2022; Curry et al., 2025).

To further identify regions approaching the observational benchmark, we define $\Delta R_{Ar}=|R_{Ar,end}-4.2|$. In addition to the reference-range cases, cases with $0.10<\Delta R_{Ar}\leqslant0.30$ are classified as near-reference, those with $0.30<\Delta R_{Ar}\leqslant0.60$ as intermediate, and the remaining cases as distant. These categories describe only the proximity of the simulated endpoint to the observational benchmark and are used to identify regions requiring higher sampling resolution. They do not represent probabilities, statistical significance, or confidence levels.

Local parameter refinement is performed for the reference-range and near-reference cases identified in the global survey, following the sampling scheme summarized in Table 2. For cases near the boundaries of the global grid, the refinement is allowed to extend beyond the original parameter limits. This refinement increases the sampling resolution within regions identified by the global survey rather than providing a uniform exhaustive search of the entire parameter space. Subsequent interpretation of Ar isotope fractionation and comparisons among the solar evolutionary tracks are therefore restricted to the parameter ranges and sampling resolution explored here.

3. Results

3.1. Benchmark against multicomponent hydrodynamic escape calculations

The numerical framework used in this study extends

Table 2 Local parameter refinement applied to reference-range and near-reference cases identified in the global survey

Global-survey category	Local sampling in P_{vol}	Local sampling in ϕ_{CO_2}
Near-reference	P_0, $P_0 \pm 2$, $P_0 \pm 5$, $P_0 \pm 10$ bar	ϕ_0, $\phi_0 \pm 0.01$, $\phi_0 \pm 0.02$
Reference-range	P_0, $P_0 \pm 1$, $P_0 \pm 2$, $P_0 \pm 5$, $P_0 \pm 10$ bar	ϕ_0, $\phi_0 \pm 0.01$, $\phi_0 \pm 0.02$

the model of Wang et al. (2025) by incorporating a diffusion-limited constraint on hydrogen escape and a heating efficiency that varies with atmospheric composition. To test whether the model reproduces the atmospheric depletion timescales obtained in previous multicomponent hydrodynamic escape calculations, we benchmark our results against those of Erkaev et al. (2014). We adopt the four initial steam-atmosphere cases A–D listed in Table 2 of Erkaev et al. (2014). The initial surface partial pressures of H_2O are 52,108,122, and 257 bar, with corresponding CO_2 partial pressures of 11, 22, 26, and 54 bar, respectively. Each initial atmosphere is combined with the four escape conditions CI–CIV from Table 3 of Erkaev et al. (2014), resulting in 16 benchmark cases. Because Erkaev et al. (2014) treated the escaping atmosphere as an H, O, and C system, whereas the present model considers an H, O, and CO_2 system, the representations and escape treatments of the carbon-bearing component are not directly equivalent. Consequently, a strict species-by-species comparison of the instantaneous escape fluxes is not appropriate. We instead use $t_{1\%}$, defined as the time required for the total atmospheric inventory to decline to 1% of its initial value, as the benchmark metric for comparing the bulk atmospheric depletion timescales predicted by the two models.

The calculated $t_{1\%}$ values agree with the atmospheric depletion timescales reported by Erkaev et al. (2014) at both ends of the initial inventory range. For the lowest-inventory case A, the A-CI and A-CIV simulations yield $t_{1\%}$ values of 2.35 and 0.423 Myr, matching the reported constraints of less than 2.5 Myr and approximately 0.4 Myr, respectively. For the highest-inventory case D, the four escape conditions produce $t_{1\%}$ values ranging from 2.09 to 11.6 Myr, which are broadly comparable to the reported range of approximately 2.1 to 12 Myr. The remaining combinations of initial atmospheric inventory and escape condition also show a similar level of agreement, as summarized in Fig. 1.

Because $t_{1\%}$ is obtained by integrating the escape history, we assessed its sensitivity to temporal resolution by repeating all 16 cases with the time step reduced from 0.001 to 0.0005 Myr. The maximum relative difference in $t_{1\%}$ between the two resolutions is only 0.00728%, indicating adequate numerical convergence. The agreement with the depletion timescales reported by Erkaev et al. (2014), together with the time-step convergence test, supports the reliability of the calculated atmospheric escape histories. These histories therefore provide the numerical basis for tracking the cumulative differential loss of ^{36}Ar and ^{38}Ar and the resulting isotopic fractionation.

3.2. Results in the global parameter space

Following the global parameter survey described in Section 2.3, we performed a total of 1,023 simulations spanning the slow-, moderate-, and fast-rotator tracks of the young Sun. Figure 2 compares the distributions of the final $^{36}Ar/^{38}Ar$ values among the three tracks. Because all simulations start from the same initial $^{36}Ar/^{38}Ar$, variations in the final ratio record the cumulative fractionation produced along each modeled atmospheric escape history.

The global survey shows that the final Ar isotopic ratio depends strongly on the evolutionary track of the young Sun. Among the 1023 simulations, only 30 produce Reference-range or Near-reference results, all under the slow- or moderate-rotator track. The slow-rotator track is the only one that produces Reference-range results, comprising all three such cases together with 10 Near-reference cases. It also yields the broadest distribution of final $^{36}Ar/^{38}Ar$ values and the strongest fractionation. The moderate-rotator track produces the remaining 17 candidate cases, all classified as Near-reference. Its results are more concentrated, with only the low-ratio end approaching the modern Martian near-surface atmospheric $^{36}Ar/^{38}Ar$ range of 4.1–4.3. By

Table 3 Mean results obtained with composition-dependent heating efficiency and fixed heating efficiency $\eta_{eff} = 0.15$. Values before and after the slash correspond to the composition-dependent and fixed-efficiency calculations, respectively. ΔL_{36-38} denotes the difference in cumulative loss fraction between ^{36}Ar and ^{38}Ar, in percentage points

Test region	Number of cases	Cases within observational range	Mean final $^{36}Ar/^{38}Ar$	Mean t_{36-38} (Myr)	Mean ΔL_{36-38}
Higher inventory – slow rotator	6	6 / 0	4.1989 / 5.3208	3.80 / 2.89	8.22 / 1.06
Lower inventory – moderate rotator	4	0 / 0	4.4043 / 4.8615	1.18 / 0.60	3.65 / 1.84

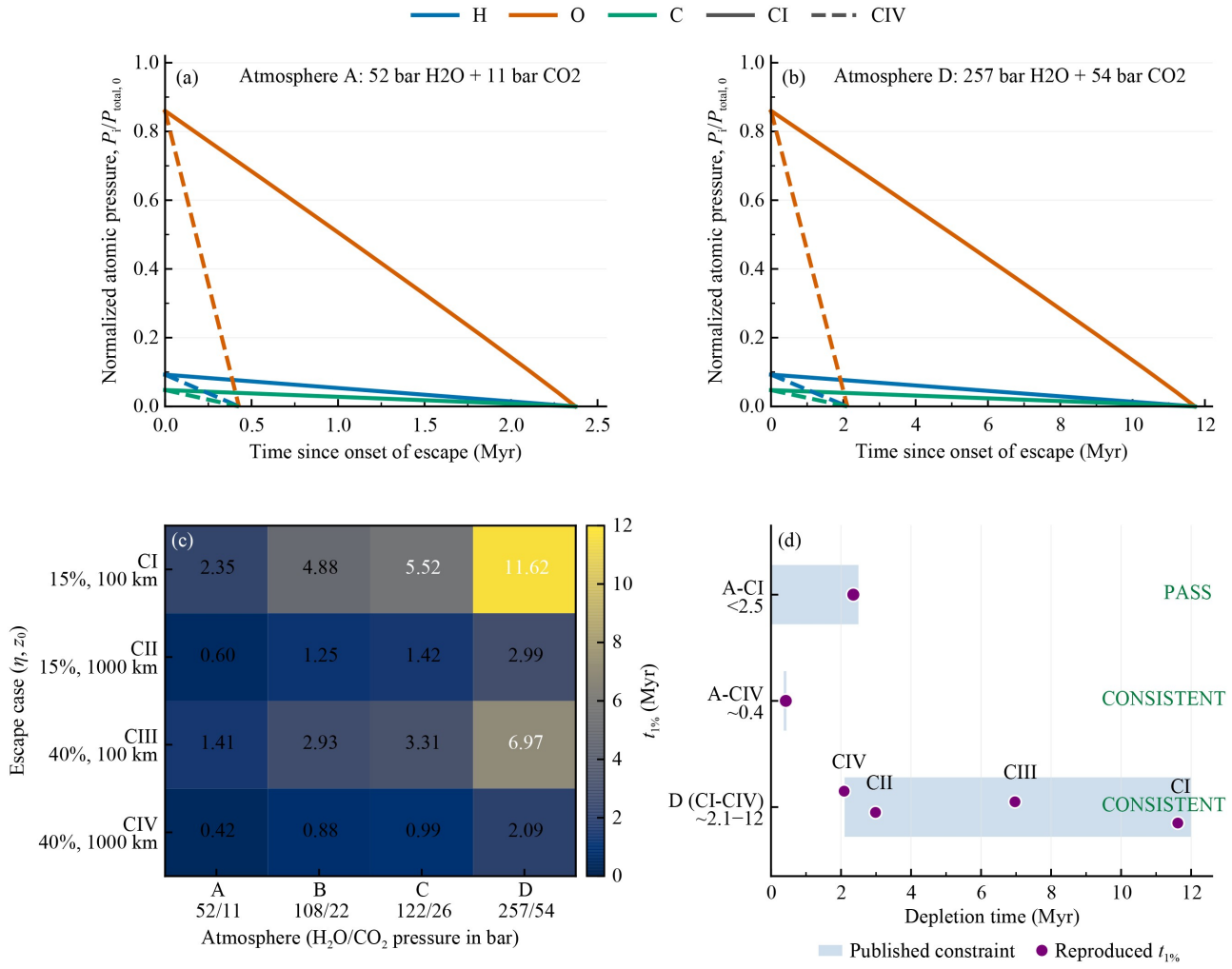

Fig. 1 Benchmark comparison between the H/O/CO_2 model used in this study and the early-Martian multicomponent escape results of Erkaev et al. (2014). (a) Temporal evolution of the atmospheric components for the low-inventory atmosphere A under CI (solid lines) and CIV (dashed lines) conditions; (b) temporal evolution of the atmospheric components for the high-inventory atmosphere D under CI (solid lines) and CIV (dashed lines) conditions; (c) depletion time $t_{1\%}$ required for the total inventory of the four initial atmospheres to decrease to 1% of its initial value under CI–CIV conditions; (d) comparison between the $t_{1\%}$ values calculated in this study and the characteristic depletion-timescale ranges reported by Erkaev et al. (2014). The time t denotes elapsed time since the onset of escape rather than the absolute model time; $t = 0$ corresponds to the adopted escape onset time of 10 Myr.

contrast, the fast-rotator track produces no candidate cases. This limited fractionation is consistent with stronger EUV forcing, under which sufficiently strong hydrogen outflow can entrain both ^{36}Ar and ^{38}Ar efficiently, thereby reducing their differential escape.

To identify the initial atmospheric conditions associated with these 30 candidate cases, Fig. 3 maps the final ^{36}Ar/^{38}Ar values onto the global parameter space defined by the initial total volatile pressure, P_{vol}, and the initial CO_2 pressure fraction, ϕ_{CO_2}. Under the slow-rotator track, the Reference-range and Near-reference cases occur mainly at P_{vol} values of approximately 290–400 bar and ϕ_{CO_2} values of approximately 0.12–0.30. Under the moderate-rotator track, all candidate cases are classified as Near-reference and occur mainly at P_{vol} values of approximately 190–230 bar and ϕ_{CO_2} values of approximately 0.14–0.28. These cases form a relatively continuous candidate region on the global grid. No Reference-range or Near-reference cases occur under the fast-rotator track, and no corresponding candidate region is therefore identified. The candidate regions under the slow- and moderate-rotator tracks overlap substantially in ϕ_{CO_2} but are separated in P_{vol}.

Overall, Figs. 2 and 3 show that the final ^{36}Ar/^{38}Ar depends on both the young-Sun irradiation history and the initial atmospheric conditions. However, these candidate regions should not be interpreted as a unique reconstruction of the initial Martian atmosphere. Subsequent sputtering, ion escape, and other nonthermal escape processes may further modify the abundance and

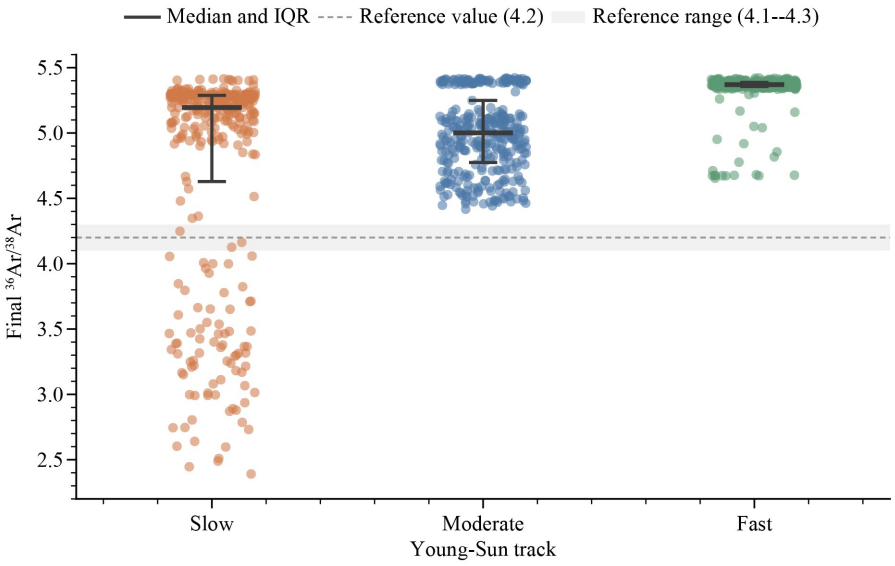

Fig. 2 Statistical distribution of the final $^{36}Ar/^{38}Ar$ under different young-Sun evolutionary tracks in the global search. Each point represents one global-search case. The horizontal axis denotes the slow-, moderate- and fast-rotator young-Sun tracks, and the vertical axis gives the final $^{36}Ar/^{38}Ar$. The gray shaded region indicates the modern near-surface Martian observational range of $^{36}Ar/^{38}Ar = 4.1$–4.3, and the dashed line marks the reference value of 4.2. Black markers indicate the median and interquartile range (IQR) for each track.

isotopic composition of Ar. These regions therefore identify only the initial conditions that yield Reference-range or Near-reference $^{36}Ar/^{38}Ar$ values at the end of the modeled hydrodynamic escape phase.

In Section 3.3, we refine the candidate regions under the slow- and moderate-rotator tracks to characterize more precisely how Ar isotopic fractionation varies with the initial atmospheric inventory and composition.

3.3. Results in the local parameter space

Following the local refinement scheme described in Section 2.3, we conducted additional simulations within the parameter ranges associated with the Reference-range and Near-reference cases identified under the moderate- and slow-rotator tracks. The refined survey comprises 257 moderate-rotator cases and 356 slow-rotator cases, giving a total of 613 unique simulations. Because the fast-rotator track produced no Reference-range or Near-reference cases in the global survey, it was not further refined. Figure 4 compares the overall distributions of the final $^{36}Ar/^{38}Ar$ values under the moderate- and slow-rotator tracks.

Under the moderate-rotator track, the final $^{36}Ar/^{38}Ar$ values are concentrated primarily between approximately 4.4 and 4.6. Some cases approach the modern observational range, but the absence of Reference-range cases indicates that the cumulative Ar isotopic fractionation remains limited. In contrast, the slow-rotator results span a substantially broader range of approximately 2.4–5.4, with most values concentrated between approximately 3.6 and 4.7. Among these simulations, 32 fall within the modern observational range. The locally refined results therefore show that the slow-rotator track produces a broader range and stronger Ar isotopic fractionation than the moderate-rotator track and is the only refined track to yield Reference-range cases.

To further examine the relationship between these final Ar isotope ratios and the initial atmospheric conditions, Fig. 5 maps the locally refined results onto the P_{vol}–ϕ_{CO_2} parameter space. Under the moderate-rotator track, the Near-reference cases retain a relatively continuous distribution at the higher parameter resolution, but no cases enter the Reference range. This indicates that, within the locally explored parameter region, the Ar isotopic fractionation produced by early hydrodynamic escape is insufficient to lower the final $^{36}Ar/^{38}Ar$ to the modern Martian observational range.

By contrast, the 32 Reference-range cases obtained under the slow-rotator track form two distinct branches in parameter space. The lower-pressure branch occurs primarily at P_{vol} values of approximately 288–352 bar and ϕ_{CO_2} values of approximately 0.12–0.30, with ϕ_{CO_2} increasing with P_{vol}. The higher-pressure branch occurs primarily at P_{vol} values of approximately 360–402 bar and ϕ_{CO_2} values of approximately 0.13–0.17, with comparatively little variation in ϕ_{CO_2}.

Notably, both branches produce final $^{36}Ar/^{38}Ar$ values within the modern observational range, showing that similar cumulative isotopic fractionation can arise from different combinations of initial atmospheric inventory

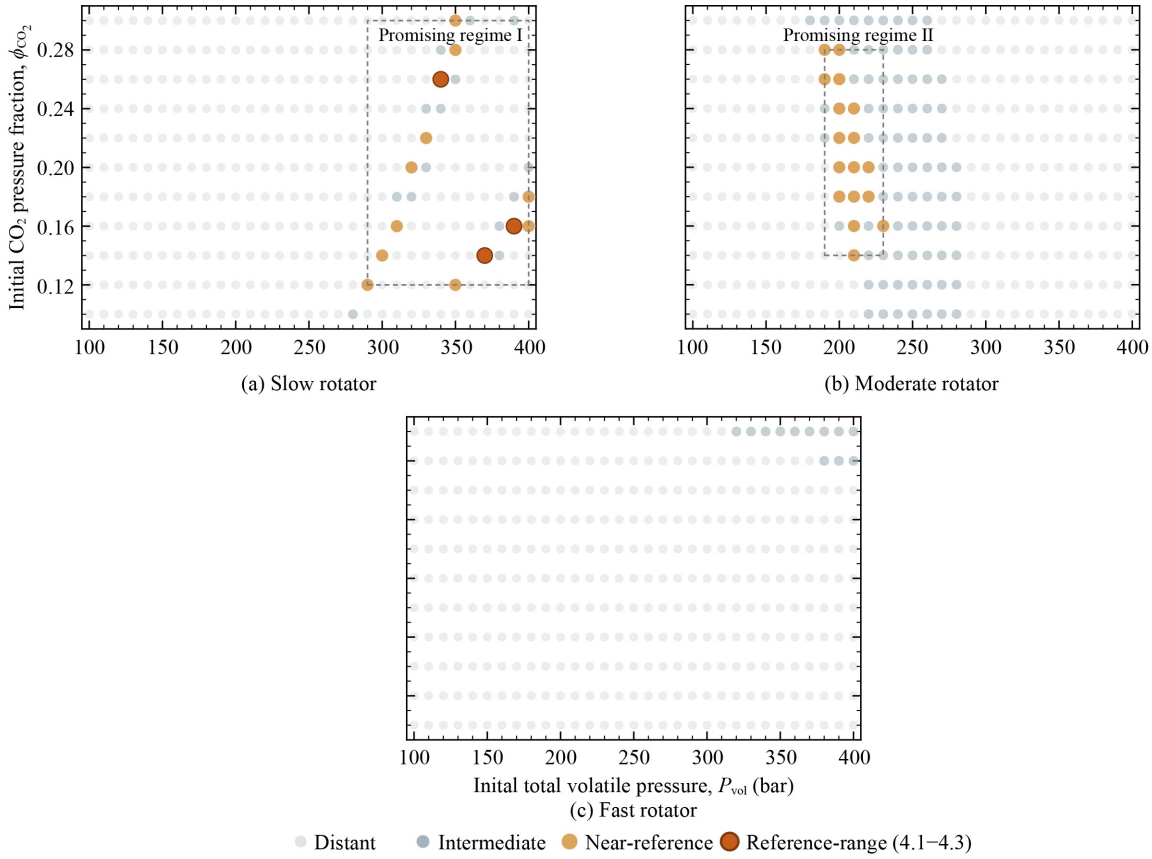

Fig. 3 Distribution of final Ar isotopic fractionation in the global parameter space under different young-Sun evolutionary tracks. (a) slow-rotator young-Sun track; (b) moderate-rotator young-Sun track; (c) fast-rotator young-Sun track. The horizontal axis is the initial total atmospheric pressure P_{vol}, and the vertical axis is the initial CO_2 pressure fraction ϕ_{CO_2}. Colors indicate the deviation of the final $^{36}Ar/^{38}Ar$ from the modern Martian reference value of 4.2 and are classified as Large deviation, Moderate deviation, Near-reference, and Reference range; the Reference range corresponds to $^{36}Ar/^{38}Ar = 4.1$–4.3. Dashed boxes indicate the regions selected for subsequent local parameter-space refinement. The dashed boxes labeled Promising regimes I and II denote the slow- and moderate-rotator candidate regions selected for local refinement, respectively.

and composition. Thus, under the slow-rotator model considered here, the final Ar isotope ratio alone does not uniquely determine the initial atmospheric parameters. Nevertheless, when the modern observational range is used as a benchmark, the compatible modeled endpoints are restricted to two relatively confined branches in parameter space.

4. Discussion

4.1. Effect of composition-dependent heating efficiency on Ar isotopic fractionation

According to the parameterization adopted in Section 2.1, the effective heating efficiency η_{eff} varies dynamically with the H_2O–CO_2 composition of the lower atmosphere. Among the cases whose final $^{36}Ar/^{38}Ar$ ratios fall within the modern Martian observational range of 4.1–4.3, we selected a representative slow-rotator case with $P_{vol} = 310$ bar and $\phi_{CO_2} = 0.165$ to examine the temporal evolution of the composition-dependent heating efficiency. In this case, as H_2O is continuously lost and the atmosphere becomes progressively enriched in CO_2, η_{eff} decreases from an initial value of 0.14692 to 0.12904 (Fig. 6). This evolution indicates that treating the heating efficiency as a fixed parameter may not fully capture the feedback of atmospheric composition on upper-atmospheric energy deposition and hydrodynamic escape.

To evaluate the effect of this composition-dependent heating-efficiency treatment on Ar isotopic fractionation, we further performed 10 control cases using either the composition-dependent η_{eff} or a fixed value of $\eta_{eff} = 0.15$. The test set comprises six representative high-volatile, slow-rotator cases (H1–H6) and four representative lower-volatile, moderate-rotator cases (L1–L4). All model parameters other than the treatment of heating efficiency are identical between the two

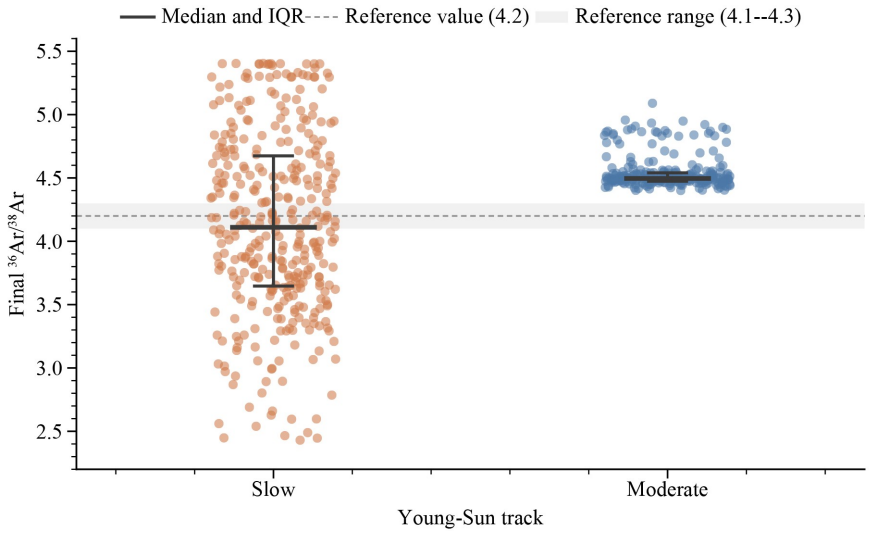

Fig. 4 Statistical distribution of the final $^{36}Ar/^{38}Ar$ under different young-Sun tracks in the locally refined search. Each point represents one local-search case. The horizontal axis denotes the slow- and moderate-rotator young-Sun tracks, and the vertical axis gives the final $^{36}Ar/^{38}Ar$. The gray shaded region indicates the modern near-surface Martian observational range of $^{36}Ar/^{38}Ar = 4.1–4.3$, and the dashed line marks the reference value of 4.2. Black markers indicate the median and interquartile range (IQR) for each track.

calculations. The comparison therefore illustrates the effect of adopting the composition-dependent heating-efficiency parameterization, although it does not fully separate the time dependence of η_{eff} from differences in its effective magnitude.

The two treatments produce distinctly different Ar isotopic fractionation outcomes (Fig. 7; Table 3). For cases H1–H6, the composition-dependent heating efficiency yields a mean final $^{36}Ar/^{38}Ar$ of 4.1989, with all six cases falling within the modern Martian observational range. With fixed $\eta_{\mathrm{eff}} = 0.15$, the mean final $^{36}Ar/^{38}Ar$ increases to 5.3208, and none of the cases falls within that range. At the same time, the cumulative duration for which the crossover mass lies within 36–38 amu, t_{36-38}, decreases from an average of 3.80 Myr to 2.89 Myr, while the difference in cumulative loss fraction between ^{36}Ar and ^{38}Ar, ΔL_{36-38}, decreases from 8.22 to 1.06 percentage points. A similar trend occurs for cases L1–L4: the fixed heating efficiency reduces the mean t_{36-38} from 1.18 Myr to 0.60 Myr and increases the mean final $^{36}Ar/^{38}Ar$ from 4.4043 to 4.8615.

These results show that the relationship between heating efficiency and the degree of Ar isotopic fractionation is not simply monotonic. A higher η_{eff} generally enhances hydrodynamic H escape and increases its ability to drag heavy species, but this does not necessarily imply stronger Ar isotopic fractionation. For ^{36}Ar and ^{38}Ar, pronounced differential escape occurs mainly when the crossover mass approaches the masses of the two isotopes. When m_c is well above 38 amu, both isotopes can be efficiently dragged and their escape behavior becomes more similar; when m_c is below 36 amu, hydrodynamic drag of both isotopes is suppressed. In contrast, when m_c lies within approximately 36–38 amu, the lighter ^{36}Ar is more readily dragged than ^{38}Ar, producing stronger isotopic selectivity.

Therefore, an important diagnostic of cumulative Ar isotopic fractionation is not the absolute heating efficiency or H escape flux at a particular instant, but the temporal history of the crossover mass entering and remaining within this selective-fractionation window during atmospheric evolution. The composition-dependent η_{eff} modifies the response of H escape to atmospheric composition and allows the crossover mass to remain within 36–38 amu for a longer duration, thereby enhancing the cumulative differential loss between ^{36}Ar and ^{38}Ar. In contrast, with fixed $\eta_{\mathrm{eff}} = 0.15$, the cumulative residence time of the crossover mass within this interval is generally shorter. Consequently, even though the energy input and H escape may be stronger, the resulting Ar isotopic fractionation is weaker.

Overall, these control calculations show that atmospheric composition affects Ar drag not only by changing the available H inventory but also by modifying the temporal evolution of the crossover mass through the composition-dependent heating efficiency. For Ar isotopes, this feedback acts mainly by regulating the residence time of m_c within the selective-fractionation window and contributing to the cumulative differential loss of ^{36}Ar and ^{38}Ar. The temporal and compositional dependence of heating efficiency may therefore be an important factor in quantitative studies of noble-gas isotopic evolution on early Mars.

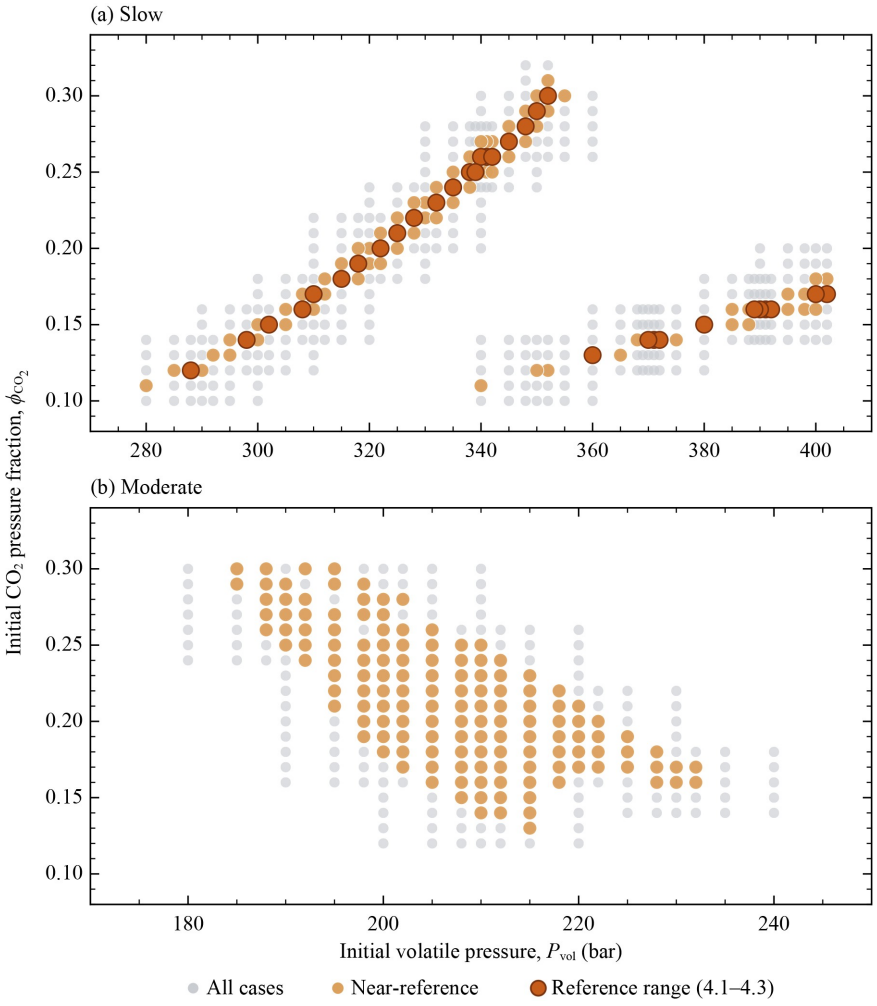

Fig. 5 Distribution of final Ar isotopic fractionation in the locally refined parameter space. (a) slow-rotator young-Sun track; (b) moderate-rotator young-Sun track. Gray points denote all local-search cases, light-orange points denote Near-reference cases, and dark-orange points denote Reference-range cases whose final $^{36}Ar/^{38}Ar$ falls within the modern Martian observational range of 4.1–4.3.

4.2. Analytical limiting-case verification of the Ar isotopic fractionation module

To further verify the numerical implementation of the newly introduced Ar isotopic fractionation calculation, we constructed a set of limiting cases with fixed crossover masses and directly compared the numerical model results with the corresponding analytical solutions. This test examines whether the mass-selective drag described by Eq. (22) is correctly implemented in the model and provides a numerical validation for subsequent comparisons of Ar isotopic fractionation under different initial atmospheric compositions. Because the masses of ^{36}Ar and ^{38}Ar are approximately 36 and 38 amu, respectively, the tests adopt crossover masses of $m_c = 35$, 37, and 50 amu. These three values correspond to the cases in which neither Ar isotope can be dragged, only ^{36}Ar can be dragged, and both Ar isotopes can be dragged, respectively.

The corresponding x_{36} and x_{38} values are first calculated from Eq. (22). For this limiting test, the integrated escape exposure is written as the dimensionless quantity $\tau = \int 4\pi r_0^2 F_H N_H^{-1}\, dt$ and normalized to $\tau = 1$. The same initial Ar isotopic ratio, $R_{Ar,0} = 5.5005$, is adopted. When the fractionation factors remain constant, the analytical solution for the normalized Ar isotopic ratio is

$$\frac{R_{Ar}}{R_{Ar,0}} = \exp[-(x_{36} - x_{38})\tau]. \tag{26}$$

The model is then run using the same m_c values and initial isotopic ratio as in the analytical calculation, and the resulting numerical values are compared with the analytical solutions (Table 4).

Table 4 shows excellent agreement between the numerical and analytical results, with a maximum rela-

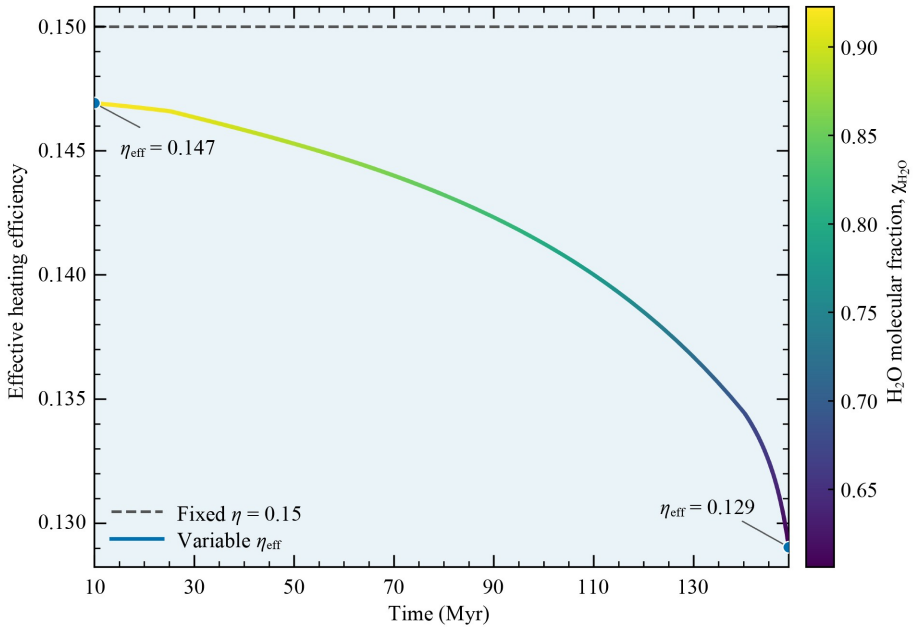

Fig. 6 Temporal evolution of the effective heating efficiency $\eta_{\rm eff}$ in the representative case. The solid curve represents the composition-dependent $\eta_{\rm eff}$, with the color along the curve indicating the lower-atmospheric H_2O mole fraction χ_{H_2O}. The horizontal dashed line denotes the fixed heating efficiency $\eta_{\rm eff}$ = 0.15 adopted in the control calculations.

tive error of only 1.08×10^{-7}. The model also correctly reproduces the expected fractionation behavior when neither Ar isotope is dragged, when only ^{36}Ar is dragged, and when both isotopes are dragged. This validation confirms that the numerical implementation reproduces the expected Ar fractionation behavior in fixed-crossover-mass limiting cases and provides a consistency check for the subsequent time-dependent calculations.

4.3. Sensitivity test of the initial Ar isotopic ratio

The baseline calculations adopt the Genesis solar-wind value $R_{\rm Ar,0}$ = 5.5005 (Meshik et al., 2014) as the initial Ar isotopic ratio. This value has also been used in discussions of the primordial Ar composition of Mars and its subsequent fractionation by atmospheric escape (Atreya et al., 2013). Given the uncertainty in the early Ar isotopic composition, we further test $R_{\rm Ar,0}$ = 5.34, 5.38, 5.42, 5.46, and 5.5005 to assess the sensitivity of the fractionation results to the initial ratio. The value 5.34 is adopted as a lower value close to the primordial meteoritic phase-Q trapped-Ar composition (Busemann et al., 2000), while the remaining values uniformly sample the interval. Three representative cases with different atmospheric compositions are re-integrated for the evolution of ^{36}Ar and ^{38}Ar, and the cumulative loss fractions of the two isotopes are compared under different initial isotopic ratios (Table 5).

The results show that changing the initial ^{36}Ar/^{38}Ar ratio has virtually no effect on the cumulative loss fractions in these representative cases. This indicates that the isotope-specific escape efficiencies are largely controlled by the escape history rather than by the assumed initial isotopic ratio. However, the final absolute ^{36}Ar/^{38}Ar ratio still scales with $R_{\rm Ar,0}$, so the classification of cases relative to the modern reference interval may shift for cases close to the 4.1–4.3 boundaries.

4.4. Complementary constraints from Ne isotopes

Ne isotopes can also undergo mass-selective fractionation during early H-driven hydrodynamic escape and could therefore provide constraints complementary to those from Ar. However, present Martian Ne is not yet a comparably robust primary constraint. The Viking Ne abundance estimate depended on indirect signal separation and an assumed isotope ratio, while no in situ measurement of atmospheric ^{20}Ne/^{22}Ne is currently available. Estimates from Martian meteorites also remain uncertain because of cosmogenic Ne and possible mantle-derived components. Moreover, the short estimated lifetime of atmospheric Ne implies that its present abundance and isotopic composition may be strongly influenced by recent escape and volcanic supply rather than solely preserving the cumulative signature of early hydrodynamic escape (Owen et al., 1977; Kurokawa et al., 2021).

This study therefore focuses on Ar isotopic fractionation under different initial atmospheric conditions and young-Sun irradiation histories, using the in situ measured modern Martian ^{36}Ar/^{38}Ar as the primary

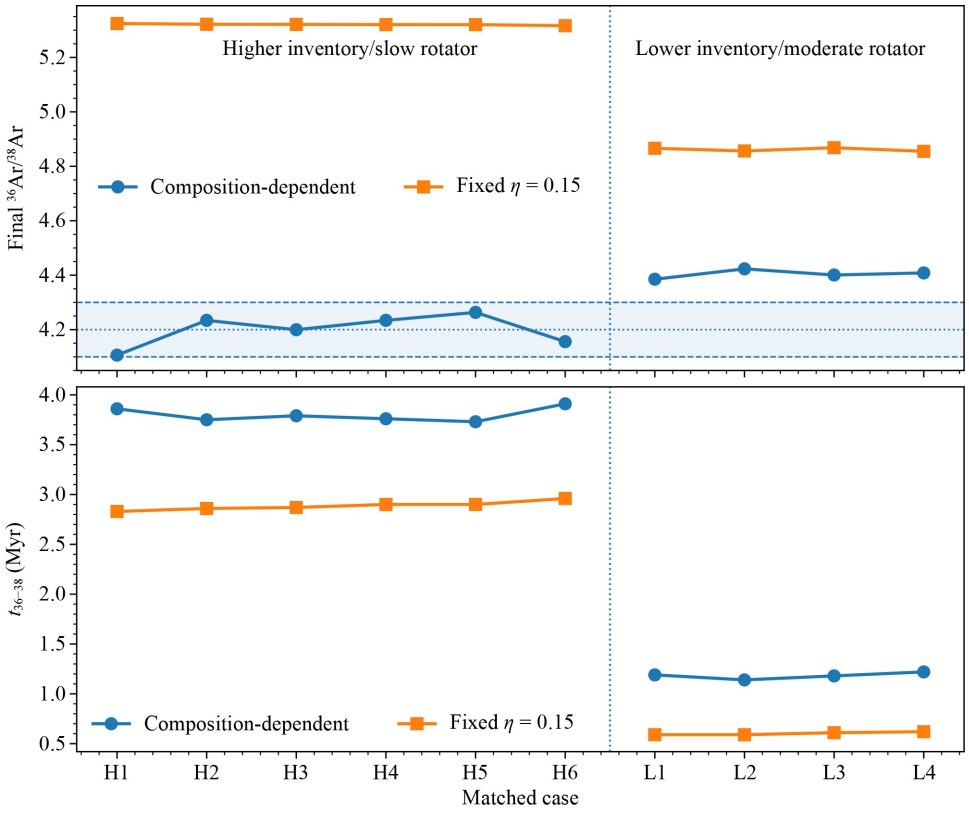

Fig. 7 Comparison of composition-dependent heating efficiency and fixed $\eta_{eff} = 0.15$ for 10 matched cases. H1–H6 denote higher-inventory slow-rotator cases, and L1–L4 denote lower-inventory moderate-rotator cases; each pair differs only in the heating-efficiency treatment. The upper panel shows the final $^{36}Ar/^{38}Ar$, with horizontal lines marking 4.2 and the observational range of 4.1–4.3. The lower panel shows the cumulative time $t_{36–38}$ for which the Ar crossover mass lies within 36–38 amu. The vertical dotted line separates the two case groups.

Table 4 Comparison of analytical and numerical Ar isotopic fractionation results under different crossover-mass conditions

Case	m_c (amu)	x_{36} (analytical/numerical)	x_{38} (analytical/numerical)	$R_{Ar}/R_{Ar,0}$ (analytical/numerical)	Relative error
A	35	0 / 0	0 / 0	1.000000000 / 1.000000000	0
B	37	0.02777778 / 0.02777778	0 / 0	0.972604477 / 0.972604473	3.86×10^{-9}
C	50	0.28571429 / 0.28571429	0.24489796 / 0.24489796	0.960005441 / 0.960005337	1.08×10^{-7}

Table 5 Cumulative Ar loss fractions for three representative cases under different initial Ar isotopic ratios

Representative case	Metric	$R_{Ar,0} = 5.34$	$R_{Ar,0} = 5.38$	$R_{Ar,0} = 5.42$	$R_{Ar,0} = 5.46$	$R_{Ar,0} = 5.5005$
SLOW, $P_{vol} = 270$ bar $\phi_{CO_2} = 0.16$	^{36}Ar loss fraction (%)	62.2809	62.2809	62.2809	62.2809	62.2809
	^{38}Ar loss fraction (%)	60.9565	60.9565	60.9565	60.9565	60.9565
	ΔL_{Ar} (percentage points)	1.3244	1.3244	1.3244	1.3244	1.3244
SLOW, $P_{vol} = 310$ bar $\phi_{CO_2} = 0.165$	^{36}Ar loss fraction (%)	73.1380	73.1380	73.1380	73.1380	73.1380
	^{38}Ar loss fraction (%)	64.0208	64.0208	64.0208	64.0208	64.0208
	ΔL_{Ar} (percentage points)	9.1172	9.1172	9.1172	9.1172	9.1172
MODERATE, $P_{vol} = 203$ bar $\phi_{CO_2} = 0.1724$	^{36}Ar loss fraction (%)	85.5747	85.5747	85.5747	85.5747	85.5747
	^{38}Ar loss fraction (%)	81.9069	81.9069	81.9069	81.9069	81.9069
	ΔL_{Ar} (percentage points)	3.6677	3.6677	3.6677	3.6677	3.6677

observational reference (Atreya et al., 2013). Improved constraints on the abundance, isotopic composition, and early inventory of Martian Ne would allow Ne and Ar to be used jointly to distinguish among different initial atmospheric conditions and escape histories.

5. Conclusions

We developed an early-Martian atmospheric evolution model that couples a 1D radiative–convective atmospheric structure with H–O–CO_2 multicomponent hydrodynamic escape. This model includes energy- and diffusion-limited H escape, mass-selective drag of Ar isotopes, and an effective heating efficiency that varies with atmospheric composition. We explored the effects of the initial total volatile pressure P_{vol}, the initial CO_2 pressure fraction ϕ_{CO_2}, and the young-Sun rotational history through a global survey of 1023 cases across three rotational tracks. This was followed by 613 locally refined cases in candidate regions under the moderate- and slow-rotator tracks. The results were evaluated against the modern Martian near-surface atmospheric value $^{36}Ar/^{38}Ar = 4.2 \pm 0.1$.

The global survey shows that the young-Sun rotational history strongly influences the final Ar isotopic fractionation. The slow-rotator track produces the broadest $^{36}Ar/^{38}Ar$ distribution, extending to the strongest fractionation, whereas the moderate- and fast-rotator results remain concentrated at higher ratios. Because the fast-rotator track yields no Reference-range or Near-reference cases, candidate regions for local refinement were identified only under the moderate- and slow-rotator tracks.

The local refinement further shows that some moderate-rotator cases approach the modern observational range, but none enter the Reference-range category. In contrast, 32 slow-rotator cases fall within the modern range and form two relatively confined branches in parameter space: a lower-pressure branch at $P_{vol} \approx$ 288–352 bar with $\phi_{CO_2} \approx 0.12$–0.30, and a higher-pressure branch at $P_{vol} \approx 360$–402 bar with $\phi_{CO_2} \approx 0.13$–0.17. Within the sampled parameter space, early hydrodynamic escape therefore produces modeled early-stage end-state Ar isotope ratios compatible with the modern observational reference only for a subset of initial atmospheric conditions under the slow-rotator track. Although the modeled early-stage Ar isotope ratio cannot uniquely recover the initial atmospheric state, it identifies two restricted regions of compatible atmospheric inventory and composition in the present model.

Comparing calculations using different treatments of heating efficiency further shows that feedback between atmospheric composition and escape can influence the predicted Ar isotopic fractionation. The numerical scheme reproduces the analytical solutions for three crossover-mass limiting cases, while the cumulative loss fractions remain essentially unchanged across the tested initial $^{36}Ar/^{38}Ar$ ratios. These tests support the reliability and robustness of the fractionation calculations while identifying the treatment of heating efficiency as a source of model dependence.

Finally, the systematic parameter survey jointly explores the effects of the young-Sun irradiation history and the initial atmospheric inventory and composition, and demonstrates that early hydrodynamic escape is a quantitatively viable mechanism for producing the observed magnitude of Martian Ar isotopic fractionation. The present model does not include subsequent non-thermal processes such as ion escape, sputtering, or photochemical escape. Nevertheless, the modeled early-stage end states characterize the potential contribution of the hydrodynamic-escape phase and provide a basis for examining its connection with subsequent atmospheric evolution. In future work, we will incorporate non-thermal escape and volcanic outgassing to construct a continuous model of Martian Ar evolution.

Appendix. Main model parameters

Table A1 Main model parameters and adopted values or ranges

Parameter	Symbol	Adopted value/range
Total atmospheric pressure in global search	P_{vol}	100–400 bar
Initial CO_2 pressure fraction in global search	ϕ_{CO_2}	0.10–0.30
Total atmospheric pressure in local search	P_{vol}	MODERATE: 180–240 bar; SLOW: 280–402 bar
Initial CO_2 pressure fraction in local search	ϕ_{CO_2}	MODERATE: 0.12–0.30; SLOW: 0.10–0.32
Initial Ar isotopic ratio	$R_{Ar,0}$	5.5005
Young-Sun evolutionary track	—	SLOW, MODERATE, FAST (Tu et al., 2015); $F_{EUV}(t) = L_{EUV}(t)/(4\pi d_{Mars}^2)$, where $L_{EUV}(t)$ follows the young-Sun evolutionary tracks of Tu et al. (2015)
Onset time of atmospheric escape	t_0	10 Myr

References

Atreya, S. K., Trainer, M. G., Franz, H. B., et al (2013). Primordial argon isotope fractionation in the atmosphere of Mars measured by the SAM instrument on Curiosity and implications for atmospheric loss. Geophysical Research Letters, 40(21): 5605–5609

Benedikt, M. R., Scherf, M., Lammer, H., et al (2020). Escape of rock-forming volatile elements and noble gases from planetary embryos. Icarus, 347: 113772

Busemann, H., Baur, H., and Wieler, R. (2000). Primordial noble gases in "phase Q" in carbonaceous and ordinary chondrites studied by closed-system stepped etching. Meteoritics & Planetary Science, 35(5): 949–973

Curry, S. M., Hara, T., Luhmann, J. G., et al (2025). First direct observations of atmospheric sputtering at Mars. Science Advances, 11(22): eadt1538

Elkins-Tanton, L. T. (2008). Linked magma ocean solidification and atmospheric growth for Earth and Mars. Earth and Planetary Science Letters, 271(1–4): 181–191

Erkaev, N. V., Lammer, H., Elkins-Tanton, L. T., et al (2014). Escape of the Martian protoatmosphere and initial water inventory. Planetary and Space Science, 98: 106–119

Hunten, D. M., Pepin, R. O., and Walker, J. C. G. (1987). Mass fractionation in hydrodynamic escape. Icarus, 69(3): 532–549

Jakosky, B. M., Slipski, M., Benna, M., et al (2017). Mars' atmospheric history derived from upper-atmosphere measurements of $^{38}Ar/^{36}Ar$. Science, 355(6332): 1408–1410

Kurokawa, H., Miura, Y. N., Sugita, S., et al (2021). Mars' atmospheric neon suggests volatile-rich primitive mantle. Icarus, 370: 114685

Lammer, H., Kasting, J. F., Chassefière, E., et al (2008). Atmospheric escape and evolution of terrestrial planets and satellites. Space Science Reviews, 139(1–4): 399–436

Lammer, H., Chassefière, E., Karatekin, Ö., et al (2013). Outgassing history and escape of the Martian atmosphere and water inventory. Space Science Reviews, 174: 113–154

Lebrun, T., Massol, H., Chassefière, E., et al (2013). Thermal evolution of an early magma ocean in interaction with the atmosphere. Journal of Geophysical Research: Planets, 118(6): 1155–1176

Lichtenegger, H. I. M., Dyadechkin, S., Scherf, M., et al (2022). Non-thermal escape of the Martian CO_2 atmosphere over time: Constrained by Ar isotopes. Icarus, 382: 115009

Lodders, K. (2021). Relative atomic Solar System abundances, mass fractions, and atomic masses of the elements and their isotopes, composition of the solar photosphere, and compositions of the major chondritic meteorite groups. Space Science Reviews, 217(3): 44

Mahaffy, P. R., Webster, C. R., Atreya, S. K., et al (2013). Abundance and isotopic composition of gases in the Martian atmosphere from the Curiosity rover. Science, 341(6143): 263–266

Marcq, E., Salvador, A., Massol, H., and Davaille, A. (2017). Thermal radiation of magma ocean planets using a 1-D radiative-convective model of H2O–CO2 atmospheres. Journal of Geophysical Research: Planets, 122(7): 1539–1553

Marrero, T. R., Mason, E. A. (1972). Gaseous diffusion coefficients. Journal of Physical and Chemical Reference Data, 1(1): 3–118

Meshik, A., Hohenberg, C., Pravdivtseva, O., and Burnett, D. (2014). Heavy noble gases in solar wind delivered by Genesis mission. Geochimica et Cosmochimica Acta, 127: 326–347

Odert, P., Lammer, H., Erkaev, N. V., et al (2018). Escape and fractionation of volatiles and noble gases from Mars-sized planetary embryos and growing protoplanets. Icarus, 307: 327–346

Owen, T., Biemann, K., Rushneck, D. R., Biller, J. E., Howarth, D. W., and Lafleur, A. L. (1977). The composition of the atmosphere at the surface of Mars. Journal of Geophysical Research, 82(28): 4635–4639

Pahlevan, K., Schaefer, L., and Porcelli, D. (2025). A hybrid origin for the Martian atmosphere. Geochemical Perspectives Letters, 34: 31–35

Slipski, M., and Jakosky, B. M. (2016). Argon isotopes as tracers for Martian atmospheric loss. Icarus, 272: 212–227

Tu, L., Johnstone, C. P., Güdel, M., and Lammer, H. (2015). The extreme ultraviolet and X-ray Sun in time: High-energy evolutionary tracks of a solar-like star. Astronomy & Astrophysics, 577: L3

Wang, Z., Zhou, Y., Liu, Y., Odert, P., and Liu, Y. (2025). Sources of hydrogen in the primordial atmosphere of Venus. Astronomy & Astrophysics, 693: A244

Watson, A. J., Donahue, T. M., and Walker, J. C. G. (1981). The dynamics of a rapidly escaping atmosphere: Applications to the evolution of Earth and Venus. Icarus, 48(2): 150–166

Willett, C. D., Cassata, W. S., and Marks, N. E. (2022). A window into atmospheric escape on early Mars provided by argon isotopes in a Martian meteorite. Geochimica et Cosmochimica Acta, 329: 119–134

Wordsworth, R. D., and Pierrehumbert, R. T. (2013). Water loss from terrestrial planets with CO_2-rich atmospheres. The Astrophysical Journal, 778(2): 154

Zahnle, K. J., and Kasting, J. F. (1986). Mass fractionation during transonic escape and implications for loss of water from Mars and Venus. Icarus, 68(3): 462–480

Zahnle, K., Kasting, J. F., and Pollack, J. B. (1990). Mass fractionation of noble gases in diffusion-limited hydrodynamic hydrogen escape. Icarus, 84(2): 502–527

Zahnle, K. J., and Kasting, J. F. (2023). Elemental and isotopic fractionation as fossils of water escape from Venus. Geochimica et Cosmochimica Acta, 361: 228–244